

HESR: A Hysteresis-Enhanced Symbolic Regression Framework for Dynamic Friction Modeling and Compensation in Robot Manipulators

Zhuoheng Li, Weihai Chen, Lei Wang, and Lijia Chen¹

Abstract—Precise friction compensation in harmonic drives is critical for high-performance robotic control, yet it remains challenged by complex nonlinear hysteresis, the rigidity of traditional physical models, and the poor out-of-distribution generalization of neural networks. We propose HESR, a novel three-stage symbolic regression framework that introduces a hysteresis-enhanced state variable to address these limitations. Driven by the ParFam-H algorithm, our approach automatically evolves explicit and interpretable friction equations. Experiments on a UFACTORY-850 manipulator demonstrate that HESR reduces Root Mean Square Error (RMSE) by over 30% compared to baselines like LuGre and RBF neural networks. Furthermore, it exhibits superior cross-frequency generalization (0.1–1.0 Hz) and decreases real-time trajectory tracking errors by 49.3%, providing a highly robust and transparent compensation strategy.

I. INTRODUCTION

The construction of precise inverse dynamics models is the cornerstone of high-performance robotic control. Although rigid-body dynamics formulations [1], [2] are well-established, significant discrepancies remain between theoretical models and physical systems due to complex joint friction. This issue is particularly acute in collaborative robots utilizing harmonic drives, where flexspline deformation and gear meshing introduce nonlinear stiffness and position-dependent torque ripples [3]. These factors couple with friction, resulting in pronounced hysteretic effects that are comprehensively analyzed in classical mechatronic studies [18], yet remain notoriously difficult to model [22].

Current friction compensation strategies face a fundamental trade-off between accuracy and interpretability, a challenge that continues to drive recent advancements in continuous dynamic modeling for high-precision tasks [20]. Conventional model-based approaches [4], [5] offer physical insight but struggle to capture the complex, coupled nonlinearities of harmonic drives due to their rigid structures. Conversely, data-driven methods, such as neural networks [6], [15], [23], achieve high approximation accuracy but function as “black boxes,” often generalizing poorly to out-of-distribution motion frequencies.

To bridge this gap, Symbolic Regression (SR) has emerged as a promising tool for discovering explicit physical laws from data [9], [10]. However, existing SR applications in robotics are largely limited to static friction mappings [11], failing to account for the dynamic hysteresis loops observed

during velocity reversals. Furthermore, traditional GP-based SR suffers from computational inefficiency and equation bloating [12], hindering the discovery of compact models for complex dynamic systems.

Addressing these limitations, this paper proposes HESR, a hysteresis-enhanced symbolic regression framework. We introduce a novel three-stage optimization pipeline that replaces traditional GP with the gradient-based ParFam algorithm [13]. Crucially, we incorporate a physics-informed hysteresis state variable as prior knowledge, enabling the automatic evolution of explicit, compact equations capable of capturing non-local memory effects. Extensive experiments on the first three joints of a UFACTORY-850 manipulator demonstrate that ParFam-H significantly outperforms traditional physical models and neural networks in both predictive accuracy and cross-frequency generalization capabilities.

The HESR methodology (Fig. 1) utilizes a UFACTORY-850 platform for data collection and comprises a three-part pipeline: 1) data preprocessing and rigid-body decoupling; 2) ParFam-H optimization for evolving the hysteresis-enhanced friction equation; and 3) comprehensive experimental validation. The remainder of this paper is organized as follows: Section II reviews related work. Section III details the rigid-body dynamics identification and friction decoupling process. Section IV introduces the proposed HESR methodology. Section V provides comprehensive experimental validation, and Section VI concludes the paper.

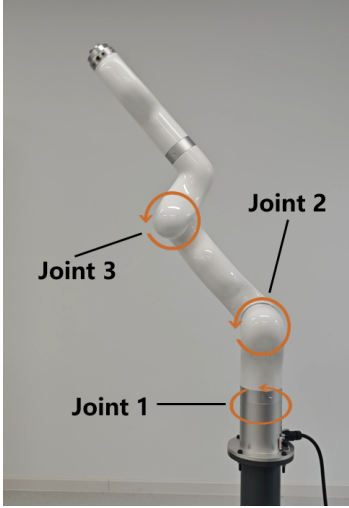
II. RELATED WORK

A. Rigid Body Dynamics Identification

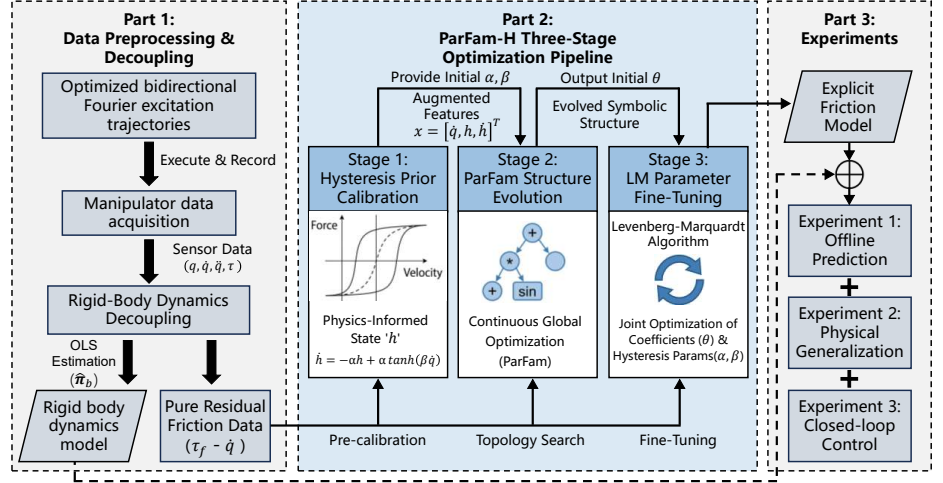
Accurate friction modeling necessitates the isolation of friction torque from the total actuation torque, which relies on a precise rigid-body dynamics model. Typically, dynamics are derived via Newton-Euler or Lagrangian formulations and linearized into a regressor form with respect to inertial parameters. To address parameter redundancy, minimum inertial parameters are identified using QR decomposition or Singular Value Decomposition (SVD). To enhance robustness against measurement noise, optimal excitation trajectories based on finite Fourier series are widely adopted, minimizing the condition number of the observation matrix. Furthermore, to prevent nonlinear friction from contaminating the identification results, techniques such as forward-reverse average motion are commonly employed to cancel out friction terms, thereby isolating the rigid-body dynamics.

This work was supported by National Natural Science Foundation of China (No. 62573014).

¹ School of Automation Science and Electrical Engineering, Beihang University, Beijing 100191, China.



(a) UFACTORY-850 platform.



(b) HESR three-stage optimization pipeline.

Fig. 1: The overall framework of the proposed HESR methodology. (a) The 6-DOF robotic manipulator (UFACTORY-850) used for data collection. (b) The detailed modeling and validation pipeline, comprising three parts: Part 1 handles data preprocessing and rigid-body dynamics decoupling; Part 2 executes the ParFam-H optimization (including hysteresis prior calibration, structure evolution, and parameter fine-tuning) to discover the explicit friction model; and Part 3 conducts experimental evaluation.

B. Friction Modeling Strategies

Friction modeling is generally categorized into static and dynamic approaches. Static models, such as the Stribeck model [14], assume friction depends solely on velocity, failing to capture position-dependent effects and dynamic memory. To address this, dynamic models like the LuGre model [5] introduce an internal state variable z , representing the average deflection of bristles between contact surfaces. The friction torque τ_f is modeled as:

$$\tau_f = \sigma_0 z + \sigma_1 \dot{z} + \sigma_2 \dot{q} \quad (1)$$

where σ_0 , σ_1 , and σ_2 represent the stiffness coefficient, microscopic damping coefficient, and viscous friction coefficient, respectively. The evolution of the bristle state z is governed by:

$$\dot{z} = \dot{q} - \frac{\sigma_0 |\dot{q}|}{g(\dot{q})} z \quad (2)$$

Here, the function $g(\dot{q})$ captures the Stribeck effect:

$$g(\dot{q}) = F_c + (F_s - F_c) e^{-(\dot{q}/v_s)^2} \quad (3)$$

where F_c is Coulomb friction, F_s is static friction, and v_s is the Stribeck velocity. While the LuGre model unifies pre-sliding, hysteresis, and steady-state characteristics, its fixed mathematical structure limits its flexibility in modeling the complex, coupled nonlinearities specific to harmonic drives.

Conversely, data-driven approaches primarily rely on Neural Networks (NN) [6], [7], [8] due to their universal approximation capabilities. Various architectures have been employed to model friction, ranging from Radial Basis Function Neural Networks (RBFNN) for static mapping to Recurrent Neural Networks (RNN) and Long Short-Term

Memory (LSTM) networks [15], [16] for capturing dynamic hysteresis. Despite their high accuracy, these methods operate essentially as “black-box” models lacking physical explainability. While recent Physics-Informed Neural Network (PINN) approaches attempt to embed physical constraints into friction-inclusive dynamics [19], achieving high-fidelity fitting still often necessitates deep or recurrent structures, imposing significant computational burdens that challenge their deployment in high-frequency real-time controllers.

C. Symbolic Regression in Robotics

Symbolic Regression (SR) bridges mechanistic and data-driven methods by discovering explicit, interpretable analytical equations from data. Recently, SR has been explored for robot inverse dynamics [17] and physical law discovery, with cutting-edge frameworks demonstrating its potential for data-efficient adaptive control in real-world robotics [21]. However, most existing SR applications rely on Genetic Programming (GP), which suffers from slow convergence and a tendency to produce bloated formulas. Critically, current SR research in friction modeling typically establishes only static mappings [24], lacking mechanisms to handle dynamic hysteresis. The memory effect near velocity zero-crossings is vital for high-precision force control but remains unaddressed by simple static SR. To overcome these limitations, this work combines physics-informed priors (hysteresis states) with the gradient-based ParFam algorithm to achieve dynamic friction modeling that is both accurate and interpretable.

III. RIGID-BODY DYNAMICS IDENTIFICATION AND FRICTION DECOUPLING

To isolate the complex nonlinear friction dynamics from the total actuation torque for subsequent symbolic regression modeling, a highly accurate rigid-body inverse dynamics model must first be established. This section outlines the dynamics linearization, excitation trajectory design, and parameter identification process.

A. Dynamics Modeling and Linearization

For the spatial 3-DOF manipulator configuration investigated in this study, the rigid-body dynamics are described by the standard Euler-Lagrange equation:

$$\mathbf{M}(\mathbf{q})\ddot{\mathbf{q}} + \mathbf{C}(\mathbf{q}, \dot{\mathbf{q}})\dot{\mathbf{q}} + \mathbf{G}(\mathbf{q}) = \boldsymbol{\tau}_{rb} \quad (4)$$

where $\mathbf{q}, \dot{\mathbf{q}}, \ddot{\mathbf{q}} \in \mathbb{R}^3$ are the joint position, velocity, and acceleration vectors, respectively. $\mathbf{M}(\mathbf{q})$ is the inertia matrix, $\mathbf{C}(\mathbf{q}, \dot{\mathbf{q}})$ contains Coriolis and centrifugal terms, $\mathbf{G}(\mathbf{q})$ represents gravity, and $\boldsymbol{\tau}_{rb}$ is the rigid-body torque.

Exploiting the linear property of robot dynamics with respect to inertial parameters, (4) can be rewritten in a regressor form:

$$\mathbf{Y}(\mathbf{q}, \dot{\mathbf{q}}, \ddot{\mathbf{q}})\boldsymbol{\pi} = \boldsymbol{\tau}_{rb} \quad (5)$$

where $\boldsymbol{\pi} \in \mathbb{R}^{30}$ is the standard inertial parameter vector (including mass, center of mass, and inertia tensor components for each link), and \mathbf{Y} is the regression matrix.

Due to kinematic constraints, linear dependencies exist within $\boldsymbol{\pi}$, making direct Least Squares estimation ill-posed. Therefore, a minimum parameter set $\boldsymbol{\pi}_b$ must be extracted. By constructing an extended observation matrix using randomly generated valid joint states, we employ numerical QR decomposition to eliminate redundant columns. For our spatial 3-DOF configuration, the original 30 standard parameters are reduced to a base set of 15 parameters. The minimal dynamics model is thus formulated as:

$$\mathbf{Y}_b(\mathbf{q}, \dot{\mathbf{q}}, \ddot{\mathbf{q}})\boldsymbol{\pi}_b = \boldsymbol{\tau}_{rb} \quad (6)$$

B. Excitation Trajectory and Decoupling

To enhance the robustness of parameter identification against measurement noise, finite Fourier series are adopted to construct periodic excitation trajectories. The full observation matrix \mathbf{W}_b is constructed by vertically stacking the regressor \mathbf{Y}_b calculated at each sampling instant along the trajectory. Consequently, the fundamental frequency and Fourier coefficients are optimized by minimizing the condition number of \mathbf{W}_b .

During the estimation phase, a forward-reverse symmetric motion strategy is implemented to decouple friction from the rigid-body dynamics. The manipulator is controlled to execute a forward trajectory $\mathbf{q}^+(t)$ and its time-reversed counterpart $\mathbf{q}^-(t)$. Theoretically, the odd-symmetric nature of friction with respect to velocity allows it to be canceled out by averaging the torques from both directions.

However, due to nonlinear hysteresis effects, the friction torque exhibits significant time delay and asymmetry near velocity zero-crossings. To address this, we introduce a data

screening mechanism during the decoupling process: data points corresponding to near-zero velocities are deliberately discarded. By retaining only the data segments with well-preserved friction symmetry, the high-confidence rigid-body torque $\bar{\boldsymbol{\tau}}_{rb}$ is obtained. Finally, the optimal estimate of the base parameters $\hat{\boldsymbol{\pi}}_b$ is computed using Ordinary Least Squares (OLS):

$$\hat{\boldsymbol{\pi}}_b = (\mathbf{W}_b^\top \mathbf{W}_b)^{-1} \mathbf{W}_b^\top \bar{\boldsymbol{\tau}}_{rb} \quad (7)$$

Once $\hat{\boldsymbol{\pi}}_b$ is precisely determined, we can extract the high-fidelity residual friction data. Specifically, utilizing the identified $\hat{\boldsymbol{\pi}}_b$ and the regressor matrix \mathbf{Y}_b , data is collected under a continuous sinusoidal sweep trajectory with varying frequencies and amplitudes. Assuming the measurement noise follows a zero-mean Gaussian distribution, the residual friction torque $\boldsymbol{\tau}_f$ is explicitly decoupled by:

$$\boldsymbol{\tau}_f = \boldsymbol{\tau}_{meas} - \mathbf{Y}_b(\mathbf{q}, \dot{\mathbf{q}}, \ddot{\mathbf{q}})\hat{\boldsymbol{\pi}}_b \quad (8)$$

where $\boldsymbol{\tau}_{meas}$ is the actual total torque measured via joint current feedback. This isolated residual $\boldsymbol{\tau}_f$ predominantly encapsulates Coulomb, viscous, and complex nonlinear hysteresis friction, serving as the pure data foundation for the subsequent modeling.

IV. HYSTERESIS-ENHANCED SYMBOLIC FRICTION MODELING

Having accurately decoupled the pure friction data $\boldsymbol{\tau}_f$, this section details the proposed Hysteresis-Enhanced Symbolic Regression (HESR) framework. To overcome the structural rigidity of conventional parametric models and the lack of interpretability in data-driven neural networks, HESR formulates the modeling process as a systematic three-stage optimization pipeline: 1) *Hysteresis Prior Pre-calibration*, where the shape parameters (α and β) of the physics-informed hysteresis state variable are pre-calibrated for each joint to capture non-local memory effects; 2) *Symbolic Structure Evolution*, utilizing the continuous global optimization-based ParFam algorithm to automatically discover an explicit, compact, and mathematically interpretable friction equation; and 3) *Parameter Fine-Tuning*, employing the Levenberg-Marquardt (LM) algorithm to globally refine all numerical coefficients for maximum predictive accuracy.

A. Hysteresis State Formulation

Most existing symbolic regression or parametric models rely solely on joint velocity \dot{q} as the input, implicitly assuming a static mapping $\tau_f = f(\dot{q})$. This assumption fails to capture the non-local memory effects in actual harmonic drives, where structural deformation causes a ‘‘hysteresis loop.’’ To overcome the multi-value mapping problem at velocity zero-crossings without introducing the structural complexity of the LuGre model, we propose a concise, physics-informed hysteresis state variable h , governed by the following first-order nonlinear differential equation:

$$\dot{h} = -\alpha h + \alpha \tanh(\beta \dot{q}) \quad (9)$$

where $\alpha > 0$ and $\beta > 0$ are tunable physical parameters. In a discrete real-time control system with sampling time Δt , the state is iteratively updated via first-order Euler discretization:

$$h_k = (1 - \alpha\Delta t)h_{k-1} + \alpha\Delta t \tanh(\beta\dot{q}_k) \quad (10)$$

The corresponding discrete derivative is $\dot{h}_k = -\alpha h_k + \alpha \tanh(\beta\dot{q}_k)$.

The physical intuition behind (9) is twofold. First, as visually analyzed in Fig. 2, the term $\tanh(\beta\dot{q})$ replaces the discontinuous $\text{sgn}(\dot{q})$ function, where a larger β generates a steeper slope near $\dot{q} = 0$, accurately simulating the abrupt Stribeck transition from static to dynamic friction. Second, the equation acts structurally as a first-order low-pass filter. The parameter α determines the decay rate (bandwidth), encoding the depth of the “memory.” During velocity reversal ($\dot{q} \rightarrow 0$), $\tanh(\beta\dot{q}) \rightarrow 0$, and the state decays exponentially as $h_k \approx (1 - \alpha\Delta t)h_{k-1}$. This residual “inertia” prevents the state from dropping to zero instantly, effectively creating the path-dependent hysteresis loop that captures actual torque peak delays caused by micro-elastic deformations. Both h and its derivative \dot{h} are utilized as augmented features to provide crucial dynamic transition information to the regression engine.

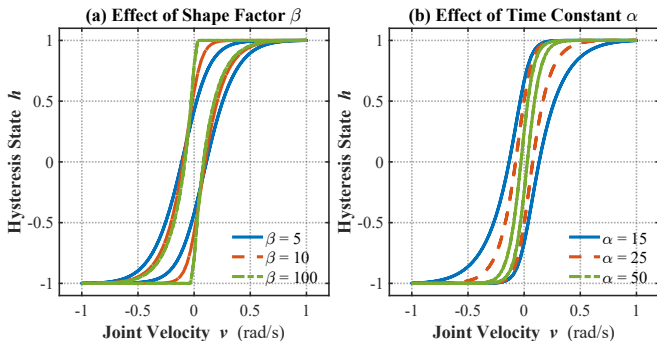


Fig. 2: Composite hysteresis analysis of the proposed friction model governed by Equation (9). (a) The shape factor β dictates the slope of the \tanh function near zero velocity. (b) The time constant α determines the decay rate of the state variable h , reflecting the memory depth and the width of the hysteresis loop.

B. Three-Stage Optimization Strategy

Friction modeling using SR is inherently a mixed-integer optimization problem involving both function topology search and parameter identification. To ensure physical consistency and avoid local optima, we propose a physics-guided three-stage optimization framework.

Stage 1: Hysteresis Prior Pre-calibration. Before feeding features into the SR algorithm, the physical parameters α and β are pre-calibrated based on genuine $\tau_f - \dot{q}$ observations. By geometrically matching the generated virtual state h to the actual hysteresis loop width and slope at velocity zero-crossings, this pre-calibration ensures the augmented input encapsulates sufficient nonlinear dynamic priors.

Stage 2: ParFam-based Global Structure Evolution.

Unlike traditional GP, which searches discrete symbolic spaces and is notoriously prone to “code bloat” and poor constant optimization, we employ the ParFam algorithm. ParFam transforms the discrete SR task into a continuous global optimization problem utilizing a Parametric Family of functions, structurally resembling a residual neural network where linear connections are replaced by rational functions Q_i and nonlinear basis functions g_i :

$$f_{\theta}(\mathbf{x}) = Q_{k+1}(\mathbf{x}, g_1(Q_1(\mathbf{x})), \dots, g_k(Q_k(\mathbf{x}))) \quad (11)$$

where $\mathbf{x} = [\dot{q}, h, \dot{h}]^T$ is the augmented input vector, and θ denotes the set of all learnable algebraic coefficients. The optimization objective is defined as:

$$\mathcal{L}(\theta) = \frac{1}{N} \sum_{i=1}^N (\tau_{f,i} - f_{\theta}(\mathbf{x}_i))^2 + \gamma \|\theta\|_1 \quad (12)$$

The L_1 regularization (coefficient γ) prunes the structure by forcing redundant coefficients to zero. We globally optimize θ via Basin-Hopping and L-BFGS-B local search. To prevent non-physical bloating, polynomial degrees are restricted to 1, cross-unit operations are prohibited, and $\mathcal{O} = \{+, -, \times, /, \sin, \cos, \exp, \tanh\}$. Finally, coefficients below a threshold are truncated, followed by BFGS refinement to yield a concise equation.

Stage 3: LM-based Global Parameter Joint Fine-Tuning.

Since the pre-calibration in Stage 1 relies on geometric observation, it inevitably introduces initial bias. Therefore, after the symbolic structure is fixed in Stage 2, we release all constraints and employ the Levenberg-Marquardt (LM) algorithm to co-optimize the physical hysteresis parameters (α, β) alongside the discovered algebraic coefficients θ as a unified set. This step eliminates cascading errors caused by pre-calibration biases, achieving a globally optimal alignment between physical priors and data-driven fitting.

V. EXPERIMENTAL EVALUATION

Experiments on the first three joints of a UFACTORY-850 cobot (harmonic drives, 200 Hz) validate the HESR framework (its evolved model is hereafter termed ParFam-H). Evaluations include: 1) Offline Prediction Accuracy against baselines; 2) Physical Generalization via out-of-distribution 0.1–1.0 Hz Chirp signals; and 3) Closed-loop Control tracking performance.

A. Experimental Setup and Baseline Identification

To isolate pure friction, rigid-body dynamics were first identified using an optimized Fourier trajectory and a forward-reverse symmetric motion strategy. Data within the velocity reversal region ($|\dot{q}| < 0.1$ rad/s) were discarded to eliminate hysteresis contamination. QR decomposition yielded 15 minimum base inertial parameters, which accurately track the macroscopic rigid-body torque (Fig. 3).

Subsequently, a sinusoidal sweep (frequency 0.25 Hz, amplitude 1.2 rad/s) was executed. By subtracting the identified rigid-body torque from the measured total torque, high-fidelity residual friction data was extracted. Finally,

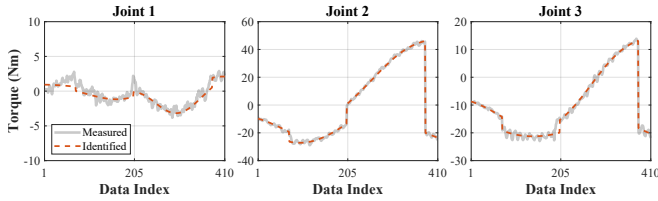


Fig. 3: Comparison of the measured total torque and the identified macroscopic rigid-body torque under the Fourier excitation trajectory.

the ParFam-H algorithm, utilizing augmented features $\mathbf{x} = [\dot{q}, h, \dot{h}]^\top$, was applied to evolve an explicit friction equation. The specific analytical formulas discovered for each joint, alongside the co-optimized physical hysteresis parameters (α, β) , are detailed in Table I.

TABLE I: Explicit Analytical Friction Equations Evolved by ParFam-H

Friction Model Equation	
Joint 1:	
$\tau_{f1} = 16.237h_1 - 0.163\dot{h}_1 - 2.128 + 37.715 \tanh(\theta_1)$	
where $\theta_1 = 0.193\dot{q}_1 - 0.606h_1 + 0.064\dot{h}_1 + 0.057$	
$(\alpha_1, \beta_1) = (11.37, 256.84)$	
Joint 2:	
$\tau_{f2} = 3.710\dot{q}_2 + 2.936h_2 + 1.220\dot{h}_2 - 0.279 + 8.290 \cos(\theta_2)$	
where $\theta_2 = -0.865\dot{q}_2 + 1.531h_2 + 0.351\dot{h}_2 + 1.485$	
$(\alpha_2, \beta_2) = (19.62, 143.91)$	
Joint 3:	
$\tau_{f3} = 0.051\dot{q}_3 + 6.614h_3 + 0.238\dot{h}_3 - 0.280 + 6.527 \tanh(\theta_3)$	
where $\theta_3 = 1.014\dot{q}_3 - 2.130h_3 + 0.115\dot{h}_3 + 0.167$	
$(\alpha_3, \beta_3) = (8.45, 278.23)$	

B. Offline Prediction Accuracy

To evaluate the fitting capability of ParFam-H on complex friction dynamics, an offline validation was conducted using an untrained, dynamically rich Fourier series trajectory (duration: 20 s, 4000 samples). Actual joint angles and torques were recorded, with velocity and acceleration derived numerically.

ParFam-H was quantitatively compared against four baselines: 1) classic LuGre and 2) Stribeck models (parameters optimized via Genetic Algorithm); 3) an RBF Neural Network (RBFNN-H), enhanced with the hysteresis state input for fair comparison; and 4) ParFam-V, an ablation symbolic model using only velocity input.

As shown in Fig. 4 and Table II, ParFam-H achieves the highest fidelity across all three joints. While traditional models (LuGre, Stribeck) yield overly smoothed predictions and RBFNN-H exhibits severe oscillations near velocity reversals, ParFam-H accurately reconstructs the transient torque peaks induced by static friction and hysteresis. The

ablation comparison with ParFam-V further proves the indispensability of the hysteresis state h for capturing reversal dynamics.

Quantitatively, ParFam-H consistently yields the lowest RMSE. For the most dynamically complex Joint 1, ParFam-H achieves an RMSE of 4.282 N·m, outperforming the sub-optimal RBFNN-H (5.186 N·m) by 17.4% and the classic LuGre model (6.370 N·m) by 32.8%. Notably, as an explicit, interpretable mathematical equation, ParFam-H surpasses the fitting-oriented black-box neural network, demonstrating an outstanding balance between predictive accuracy and physical interpretability.

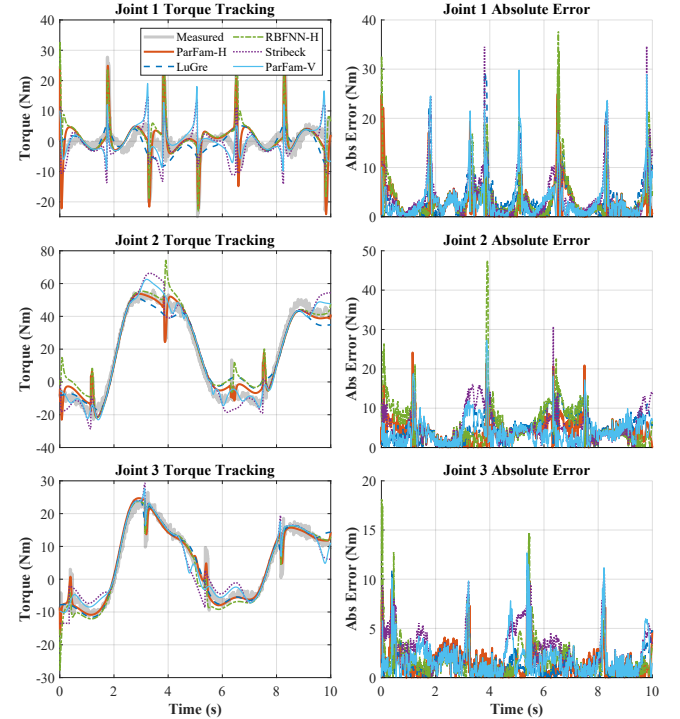


Fig. 4: Torque prediction accuracy and absolute error comparison among different friction models under an untrained, dynamically complex test trajectory.

TABLE II: Offline Torque Prediction RMSE (N·m) Comparison

Model	Joint 1	Joint 2	Joint 3
LuGre	6.3703	5.9744	2.4627
Stribeck	6.4110	6.1804	3.2741
RBFNN-H	5.1865	7.7713	2.3954
ParFam-V	6.0660	5.2261	2.6997
ParFam-H	4.2823	5.1197	1.9257

C. Physical Generalization Capability

As illustrated in Fig. 5, to assess out-of-distribution (OOD) extrapolation, a variable-frequency Chirp signal (0.1–1.0 Hz) was applied, intentionally exceeding the 0.25 Hz training frequency. The data is bisected at 0.6 Hz ($t \approx 2.6$ s) into

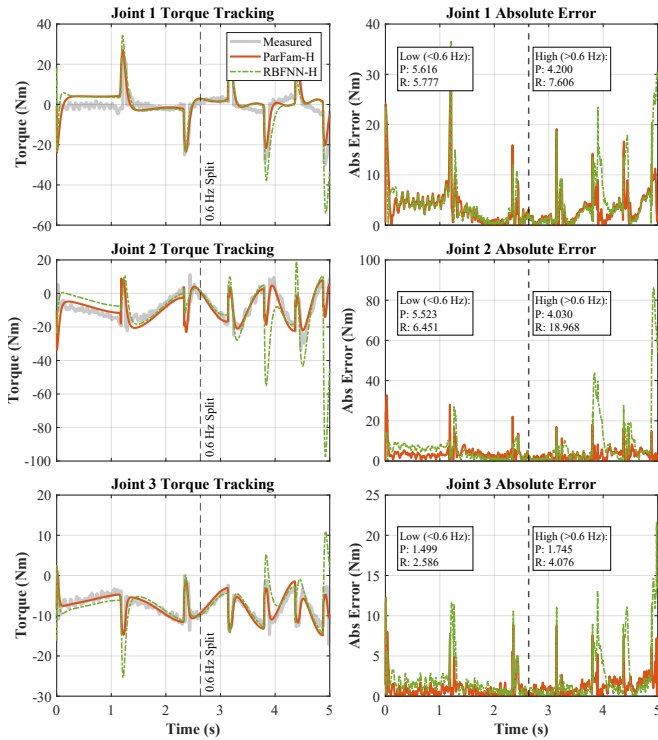


Fig. 5: Segmented frequency analysis under a variable-frequency Chirp signal. The vertical dashed line at 0.6 Hz separates the in-distribution and out-of-distribution regions. ParFam-H maintains stability in the high-frequency region, whereas RBFNN-H degrades significantly.

an in-distribution (low-frequency) region and an OOD (high-frequency) extrapolation region.

In the low-frequency region, RBFNN-H and ParFam-H exhibit comparable precision (e.g., Joint 1 RMSE: 5.777 N·m vs. 5.616 N·m), confirming the neural network’s strong in-distribution approximation ability. However, in the high-frequency region, their performances diverge drastically. The prediction error of RBFNN-H surges violently; its RMSE on Joint 2 jumps from 6.451 N·m to 18.968 N·m (a nearly $3\times$ increase). This highlights the fundamental limitation of black-box models: severe extrapolation failure when encountering unseen dynamic frequencies.

Conversely, ParFam-H maintains exceptional robustness in the high-frequency region, with its Joint 2 RMSE even decreasing from 5.523 N·m to 4.030 N·m. Observing the zero-velocity crossings, RBFNN-H suffers from severe non-physical overshoots and numerical oscillations, whereas the ParFam-H curve remains smooth and tightly tracks the measured values. This powerfully demonstrates that the evolved symbolic equations have successfully captured the frequency-invariant physical essence, enabling precise predictions far beyond the training operating points.

D. Real-time Closed-loop Control Performance

To evaluate the practical engineering utility of the ParFam-H model, dynamic trajectory tracking experiments were conducted. Since the commercial UFACTORY-850 cobot,

like most of its counterparts, restricts direct joint torque control for safety, we developed a torque-error-based adaptive velocity feedforward controller.

The core architecture utilizes the identified rigid-body and friction models to compute the theoretical total torque τ_d for the desired trajectory. The torque error $e_\tau = \tau_d - \tau_{meas}$ (where τ_{meas} is the noisy actual torque estimated from motor currents) is fed into a PD controller to generate a velocity compensation term \dot{q}_{comp} . To mitigate the amplification of high-frequency noise, an adaptive gain scheduling mechanism is introduced: the PD gains decay exponentially with respect to the desired velocity $|\dot{q}_d|$. This ensures aggressive friction compensation at low speeds (where nonlinearities dominate) and smooth, noise-suppressed motion at high speeds. The final commanded velocity sent to the robot is $\dot{q}_{cmd} = \dot{q}_d + \dot{q}_{comp}$.

Four compensation strategies were compared: Baseline (rigid-body only, no friction compensation), LuGre, RBFNN-H, and ParFam-H. As illustrated in Fig. 6, the uncompensated baseline suffers from severe phase lags and amplitude deviations during high-acceleration segments (e.g., Joint 2 at 1–3 s), confirming friction as a dominant dynamic disturbance. While all friction models improve tracking, ParFam-H achieves the tightest trajectory adherence. Notably, at $t \approx 8$ s on Joint 2, the absolute tracking error of the baseline and LuGre models exceeds 0.1 rad, whereas ParFam-H successfully suppresses the peak error to approximately 0.04 rad.

Quantitatively (Table III), ParFam-H yields the lowest RMSE across all three joints. On Joint 2, which experiences the most significant dynamic coupling and gravitational load, ParFam-H achieves an RMSE of 0.0377 rad. This represents a substantial tracking error reduction of 49.3% compared to the baseline (0.0744 rad), 38.4% against LuGre (0.0612 rad), and 21.0% against RBFNN-H (0.0477 rad). These results powerfully confirm that integrating the explicit, high-precision ParFam-H model into real-time feedforward compensation significantly enhances the precision and robustness of dynamic trajectory tracking.

TABLE III: Trajectory Tracking RMSE under Different Friction Compensation Strategies

Model	Joint 1	Joint 2	Joint 3
Baseline	0.0417	0.0744	0.0324
LuGre	0.0202	0.0612	0.0336
RBFNN-H	0.0204	0.0477	0.0267
ParFam-H	0.0177	0.0377	0.0233

VI. CONCLUSIONS AND FUTURE WORK

This paper proposes HESR, a three-stage hysteresis-enhanced symbolic regression framework for complex manipulator friction modeling. By integrating rigid-body dynamics decoupling, a physics-informed hysteresis state variable, and continuous global optimization, ParFam-H effectively overcomes the structural rigidity of traditional parametric models and the uninterpretability of black-box neural

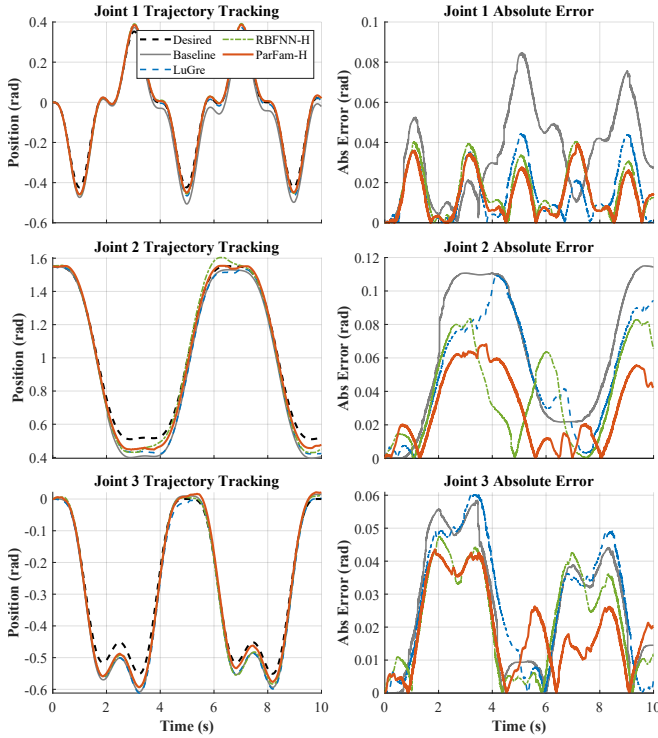


Fig. 6: Dynamic trajectory tracking performance and absolute error comparison among different controllers. ParFam-H minimizes phase lags and peak errors significantly.

networks. Experiments on a UFACTORY-850 demonstrate that the evolved explicit equations accurately capture dynamic memory effects, reducing offline torque prediction RMSE by over 30% compared to LuGre and RBFNN-H baselines. Crucially, variable-frequency Chirp tests verify its superior out-of-distribution physical generalization, strictly overcoming the severe overfitting inherent to NNs. Furthermore, integrating ParFam-H into a real-time feedforward controller reduces closed-loop trajectory tracking errors by 49.3%.

Beyond robotic friction, the introduction of the physics-informed hysteresis state variable establishes a universally applicable paradigm for symbolic regression to model systems with non-local memory effects. By effectively translating path-dependent dynamics into augmented Markovian features, this approach can be readily generalized to other complex nonlinear dynamic systems. Future work will explore the framework's robustness against varying operating conditions, specifically investigating the impact of temperature fluctuations and changing payloads on friction characteristics. To address these time-varying disturbances, we plan to integrate the explicit HESR models with online learning mechanisms to enable real-time parameter adaptation. Finally, we will investigate the transferability of the proposed methodology to other types of robotic systems governed by complex coupled dynamics, such as hydraulic actuators and flexible-joint robots.

REFERENCES

- [1] J. J. Uicker, "On the dynamic analysis of spatial linkages using 4x4 matrices," Ph.D. dissertation, Northwestern Univ., Evanston, IL, USA, 1965.
- [2] J.-J. E. Slotine, "Putting physics in control: The example of robotics," *IEEE Control Syst. Mag.*, vol. 8, no. 6, pp. 12–18, Dec. 1988.
- [3] T. D. Tuttle and W. P. Seering, "A nonlinear model of a harmonic drive gear transmission," *IEEE Trans. Robot. Autom.*, vol. 12, no. 3, pp. 368–374, Jun. 1996.
- [4] C. Canudas de Wit, H. Olsson, K. J. Astrom, and P. Lischinsky, "A new model for control of systems with friction," *IEEE Trans. Autom. Control*, vol. 40, no. 3, pp. 419–425, Mar. 1995.
- [5] J. Swevers, F. Al-Bender, C. Ganseman, and T. Prajogo, "An integrated friction model structure with improved presliding behavior for accurate friction compensation," *IEEE Trans. Autom. Control*, vol. 45, no. 4, pp. 675–686, Apr. 2000.
- [6] M. K. C. Ciliza and M. Tomizuka, "Friction modelling and compensation for motion control using hybrid neural network models," *Eng. Appl. Artif. Intell.*, vol. 20, no. 7, pp. 898–911, 2007.
- [7] K. Guo, Y. Pan, and H. Yu, "Composite learning robot control with friction compensation: A neural network-based approach," *IEEE Trans. Ind. Electron.*, vol. 66, no. 10, pp. 7841–7851, Oct. 2019.
- [8] M. Raissi, P. Perdikaris, and G. E. Karniadakis, "Physics-informed neural networks: A deep learning framework for solving forward and inverse problems involving nonlinear partial differential equations," *J. Comput. Phys.*, vol. 378, pp. 686–707, 2019.
- [9] S.-M. Udrescu and M. Tegmark, "AI Feynman: A physics-inspired method for symbolic regression," *Sci. Adv.*, vol. 6, no. 16, p. eaay2631, 2020.
- [10] B. K. Petersen *et al.*, "Deep symbolic regression: Recovering mathematical expressions from data via risk-seeking policy gradients," in *Proc. Int. Conf. Learn. Represent. (ICLR)*, 2021.
- [11] P. Scholl *et al.*, "Interpretable robotic friction learning via symbolic regression," *arXiv preprint arXiv:2505.13186*, 2025.
- [12] N. Makke and S. Chawla, "Interpretable scientific discovery with symbolic regression: A review," *Artif. Intell. Rev.*, vol. 57, no. 2, 2024.
- [13] P. Scholl *et al.*, "ParFam: (Neural guided) symbolic regression via continuous global optimization," in *Proc. Int. Conf. Learn. Represent. (ICLR)*, 2025.
- [14] B. Armstrong-Helouvry, *Control of Machines with Friction*. Boston, MA, USA: Springer, 1991.
- [15] N. Hirose and R. Tajima, "Modeling of rolling friction by recurrent neural network using LSTM," in *Proc. IEEE Int. Conf. Robot. Autom. (ICRA)*, 2017, pp. 6471–6478.
- [16] H. Yeo, J. Hong, T. Kong, and S. Oh, "Mystic-Net: MIMO hysteretic friction-aware Lagrangian-based network for legged robot," to appear in *Proc. IEEE/RSJ Int. Conf. Robot. Syst. (IROS)*, 2025.
- [17] Z. Zhang and Z. Chen, "Modeling and control of robotic manipulators based on symbolic regression," *IEEE Trans. Neural Netw. Learn. Syst.*, vol. 34, no. 5, pp. 2440–2450, 2023.
- [18] H. Zhang, S. Ahmad, and G. Liu, "Modeling of torsional compliance and hysteresis behaviors in harmonic drives," *IEEE/ASME Trans. Mechatronics*, vol. 20, no. 1, pp. 178–185, 2014.
- [19] H. Hu, Z. Shen, and C. Zhuang, "A PINN-Based Friction-Inclusive Dynamics Modeling Method for Industrial Robots," *IEEE Trans. Ind. Electron.*, vol. 72, no. 5, pp. 5136–5144, May 2025.
- [20] T. Xun, J. Yang, and H. Ding, "Improving Robotic Grinding Force Control Precision: Nonlinear Friction Compensation Based on a Novel Continuous Dynamic Model," *IEEE/ASME Trans. Mechatronics*, 2024.
- [21] E. Lee, S. A. Moore, and B. Chen, "Sym2Real: Symbolic Dynamics with Residual Learning for Data-Efficient Adaptive Control," *arXiv preprint arXiv:2509.15412*, 2025.
- [22] R. Dhaouadi, F. H. Ghorbel, and P. S. Gandhi, "A new dynamic model of hysteresis in harmonic drives," *IEEE Trans. Ind. Electron.*, vol. 50, no. 6, pp. 1165–1171, 2004.
- [23] M. Weiss, A. Pawluchin, J. H. Ewering, *et al.*, "Lagrangian Neural Network-Based Control: Improving Robotic Trajectory Tracking via Linearized Feedback," *IEEE Robot. Autom. Lett.*, vol. 11, no. 3, pp. 2546–2553, 2026.
- [24] S. B. Š, V. M., J. P. O., *et al.*, "Determining normalized friction torque of an industrial robotic manipulator using the symbolic regression method," *Industry 4.0*, vol. 8, no. 1, pp. 21–24, 2023.